Alternative route to charge density wave formation in multiband systems

Hans-Martin Eiter[a], Michela Lavagnini[a], Rudi Hackl[a,1], Elizabeth A. Nowadnick[b,c,d], Alexander F. Kemper[b,c], Thomas P. Devereaux[b,c], Jiun-Haw Chu[b,c,e], James G. Analytis[b,c,e], Ian R. Fisher[b,c,e], and Leonardo Degiorgi[f]

[a]Walther Meissner Institut, Bayerische Akademie der Wissenschaften, 85748 Garching, Germany; [b]Stanford Institute for Materials and Energy Sciences, Stanford Linear Accelerator Center, National Accelerator Laboratory, Menlo Park, CA 94025; [c]Geballe Laboratory for Advanced Materials and Departments of [d]Physics and [e]Applied Physics, Stanford University, Stanford, CA 94305; and [f]Laboratorium für Festkörperphysik, Eidgenössiche Technische Hochschule, 8093 Zürich, Switzerland

Edited by M. Brian Maple, University of California at San Diego, La Jolla, CA, and approved November 15, 2012 (received for review August 24, 2012)

Charge and spin density waves, periodic modulations of the electron, and magnetization densities, respectively, are among the most abundant and nontrivial low-temperature ordered phases in condensed matter. The ordering direction is widely believed to result from the Fermi surface topology. However, several recent studies indicate that this common view needs to be supplemented. Here, we show how an enhanced electron–lattice interaction can contribute to or even determine the selection of the ordering vector in the model charge density wave system $ErTe_3$. Our joint experimental and theoretical study allows us to establish a relation between the selection rules of the electronic light scattering spectra and the enhanced electron–phonon coupling in the vicinity of band degeneracy points. This alternative proposal for charge density wave formation may be of general relevance for driving phase transitions into other broken-symmetry ground states, particularly in multiband systems, such as the iron-based superconductors.

electron–phonon interactions | nonconventional mechanism | Raman spectroscopy | solid–solid phase transitions

The common view of charge density wave (CDW) formation was originally posed in the work by Kohn (1). Using Kohn's reasoning (1), the tendency to ordering is particularly strong in low dimensions, because the Fermi surface has parallel parts, referred to as nesting. This nesting leads to a divergence in the Lindhard susceptibility, determining the magnitude and direction of the ordering vector **Q** (2). This divergence in the electronic susceptibility is conveyed to the lattice by the electron–phonon coupling: a phonon softens to zero frequency at **Q**, and a static lattice distortion develops when the system enters the CDW state, a behavior known as the Kohn anomaly.

However, several publications raise the question as to whether nesting alone is sufficient to explain the observed ordering direction **Q** (3–7), particularly in dimensions higher than 1D. A central question is whether the selection of the CDW ordering vector is always driven by an electronic instability or if the ordering vector could, instead, be determined by a lattice distortion driven by some other mechanism exploiting the role of the electron–phonon coupling. In the latter case, the selected ordering vector would not necessarily nest the Fermi surface. The importance of strongly momentum-dependent electron–phonon coupling on CDW formation was pointed out in refs. 3 and 4, where the relevance of the Fermi surface for determining the ordering vector was indeed found to decrease as the coupling strength increases. In a recent paper on inelastic X-ray scattering measurements on 2*H*-$NbSe_2$, acoustic phonons were observed to soften to zero frequency over an extended region around the CDW ordering vector (8). The authors argue that this behavior is not consistent with a Kohn anomaly picture, where sharp dips are expected (8). Therefore, the phonon softening must be driven by another mechanism, which they identify as a wave vector-dependent electron–phonon coupling. In addition, previous studies on chromium (9) and ruthenium (10) have also shown dips in phonon dispersions arising from such anisotropic electron–phonon matrix elements.

For exploring a possible relation between anisotropic electron–phonon coupling and CDW ordering selection, it is desirable to map out the coupling strength in momentum space. For certain types of phonons, the electron–phonon matrix element is proportional to the electron–photon matrix element from Raman spectroscopy. As a result, Raman spectroscopy, which efficiently projects out different regions of the Brillouin zone with different photon polarizations, can provide an indirect method for investigating the momentum dependence of the electron–phonon coupling in a system.

To set the stage for our discussion, we introduce the 2D rare-earth tritellurides (RTe_3), which are shown in Fig. 1*A*. Among them, the prototypical $ErTe_3$ (*Materials and Methods*) undergoes a first CDW transition at $T_{CDW1} = 265$ K followed by a second one at $T_{CDW2} = 155$ K, and it allows a robust access to its intrinsic CDW properties. The ordering vectors $\mathbf{Q_1}$ and $\mathbf{Q_2}$ are parallel to but incommensurate with the reciprocal lattice vectors $c^* \parallel c$ and $a^* \parallel a$, respectively (11–20). The electronic properties of these layered CDW compounds can be modeled by considering a single Te plane (Fig. 1*B* and *SI Text*). The two dominant hopping terms are $V_{p\sigma}$ and $V_{p\pi}$ along and perpendicular to the overlapping p_x or p_z orbitals, respectively, leading to slightly warped Fermi surface planes (Fig. 1*C*). For this band structure, Yao et al. (5) studied the influence of band-filling and electron–phonon coupling strength on the charge ordering and established a strong coupling limit for the experimentally observed stripe-like CDW state. Additionally, the work by Johannes and Mazin (7) found that the Lindhard susceptibility has peaks of comparable size at the nesting vector **Q*** predicted from the band structure and the CDW ordering vector $\mathbf{Q_1}$, determined experimentally in RTe_3 (13) (Fig. 1*C*). This finding is quite similar to a recent observation in $NbSe_2$ (6). The inclusion of a small but nonzero hopping term between p_x and p_z ($V_{xz} \neq 0$) lifts the degeneracy at the intersection points of the two quasi-1D Fermi surfaces, which is emphasized in Fig. 1*D*, and improves the agreement with the experimental Fermi surface, although **Q*** remains the best nesting vector (12). Therefore, mechanisms beyond purely electronic ones have been conjectured to play an important role in selecting the ordering vector and forming the density wave. These mechanisms include orthorhombicity, the tendency to phase separation and nematicity by

Author contributions: H.-M.E., M.L., and R.H. designed research; H.-M.E., M.L., J.-H.C., J.G.A., and I.R.F. performed research; E.A.N., A.F.K., T.P.D., J.-H.C., J.G.A., and I.R.F. contributed new reagents/analytic tools; H.-M.E., M.L., R.H., E.A.N., A.F.K., T.P.D., and L.D. analyzed data; and H.-M.E., R.H., E.A.N., A.F.K., T.P.D., and L.D. wrote the paper.

The authors declare no conflict of interest.

This article is a PNAS Direct Submission.

Freely available online through the PNAS open access option.

[1]To whom correspondence should be addressed. E-mail: Rudi.Hackl@wmi.badw-muenchen.de.

This article contains supporting information online at www.pnas.org/lookup/suppl/doi:10.1073/pnas.1214745110/-/DCSupplemental.

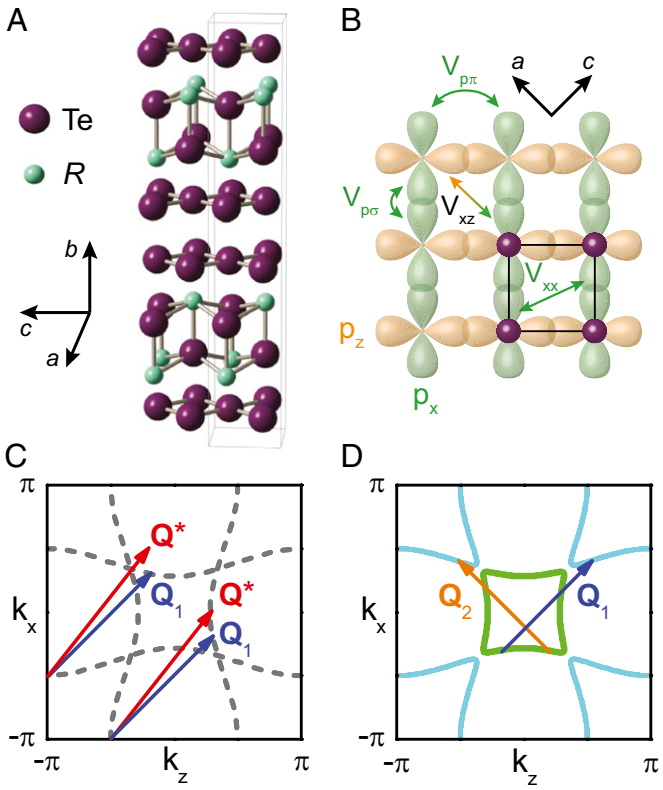

Fig. 1. Real and reciprocal space structure of rare-earth tritellurides. (*A*) Crystal structure with violet and green spheres representing tellurium and rare-earth atoms, respectively. The 3D crystallographic cell is indicated in gray. Note that the Te planes are perpendicular to the *b* axis (11). (*B*) Orbital character of the Te 5*p* orbitals in the Te plane. The unit cell is indicated by a full line. The band structure near the Fermi energy E_F is derived from the Te 5*p* orbitals. The various hopping matrix elements are indicated. (*C*) Fermi surface as derived from the p_x and p_z orbitals alone ($V_{p\sigma} = 2.99$, $V_{p\pi} = -1$, $V_{xx} = 0.09$ eV, and $V_{xz} = 0$) (details in *SI Text*). Note that only V_{xz} contributes to the hybridization. There are two energetically possible orientations for CDW ordering, $\mathbf{Q_1}$ and $\mathbf{Q^*}$, where $\mathbf{Q^*}$ is the wave vector predicted by nesting. (*D*) Theoretical Fermi surface for $V_{xz} = 0.12$ eV best reproducing the experimental findings (12). Also shown are the two experimentally observed orthogonal ordering vectors $\mathbf{Q_1}$ and $\mathbf{Q_2}$ parallel to the crystallographic *c* and *a* axes, respectively, corresponding to the CDW transitions at T_{CDW1} and T_{CDW2}.

the Coulomb interaction, strongly momentum-dependent electron–phonon interaction caused by peculiarities of the band structure, breakdown of the Coulomb screening, and other competing instabilities, such as magnetism (5, 7, 21–24).

In this research report, we analyze data from Raman experiments and the related selection rules for $ErTe_3$ and show that the lifting of band degeneracies enhances the light-scattering sensitivity and concomitantly, the electron–phonon coupling at ordering vectors that do not coincide with those vectors predicted by nesting alone.

Results

Fluctuation Regime Above the CDW Transition Temperature. We first display the low-frequency Raman spectra above T_{CDW1} in Fig. 2. The narrow lines superposed on the continuum are the Raman-active phonons of the high-temperature phase (16). Instead of the expected flat continuum (25), strongly temperature-dependent shoulders, emerging from the normal metallic response, are observed for $T_{CDW1} < T < 300$ K in the low-energy part of the spectra (Fig. 2 *A* and *B*). These excitations have similar intensity in *aa* and *cc* polarization configurations (defined in *Materials and Methods*), soften, and get stronger on approaching T_{CDW1} from higher temperatures. Above 300 K, the spectra are essentially temperature-independent, which is expected for a metal with an almost constant resistivity (13).

In Fig. 2 *C* and *D*, we show the strongly temperature-dependent parts of the spectra alone that closely follow the prediction in the work by Caprara et al. (26) for the exchange of fluctuations. A fluctuation regime, suppressing T_{CDW1} below the mean field transition temperature and out of which the CDW state emerges, is expected to exist at temperatures well above T_{CDW1}, particularly in our case, with a large ratio $2\Delta_1/k_BT_{CDW1} \sim 15$ being approximately four times the canonical mean field value of 3.53 (2). Signatures of such CDW precursor effects were, indeed, observed by X-ray diffraction (13) and optical (IR) spectroscopy (18, 20). Here, we also reveal the nature and symmetry properties of the fluctuations; our observations are compatible with the A_{1g} channel, which indicates the survival of the C_4 rotational symmetry of the pseudotetragonal phase. [The in-plane lattice parameters are almost identical; therefore, the Te planes are essentially square (C_4-symmetric), although the structure is fundamentally orthorhombic because of the glide plane between adjacent Te layers.] The survival of the C_4 rotational symmetry excludes the presence of precursor effects caused by nematic order, (e.g., intensively debated in the cuprates) (24, 27), which would appear in B_{1g} symmetry.

CDW Amplitude Mode Excitations and Electron–Phonon Coupling Strength. Immediately below T_{CDW1}, the amplitude mode (AM) of the CDW pops up and gains intensity with decreasing temperature, shown as peak-α in Fig. 3. The AM appears in both polarizations, *aa* and *cc*, with an intensity ratio of ~2:1. On additional cooling, the AM moves to higher energies, couples to phonons (19), and gains more than one order of magnitude in intensity (17). At the

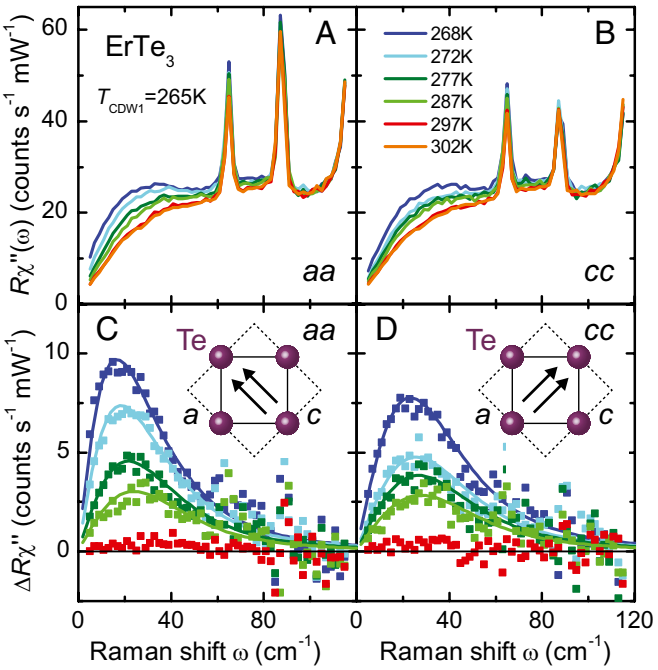

Fig. 2. Normal-state Raman scattering response of $ErTe_3$ at low energies. The imaginary part $R\chi''_{i,s}(\omega, T)$ of the Raman response is shown in *A* for *aa* and *B* for *cc* configuration, with the first and the second labels representing the polarizations $\mathbf{e}_i$ and $\mathbf{e}_s$ of the incoming and scattered photons, respectively, as indicated in *C Inset* and *D Inset*. The spectra display the presence of a fluctuation-induced response for a temperature range of about 30 K above T_{CDW1}. In *C* and *D*, the fits from ref. 26 to the fluctuation contribution $\Delta R\chi'' = R\chi''(\omega, T) - R\chi''(\omega, 302\text{ K})$ are shown.

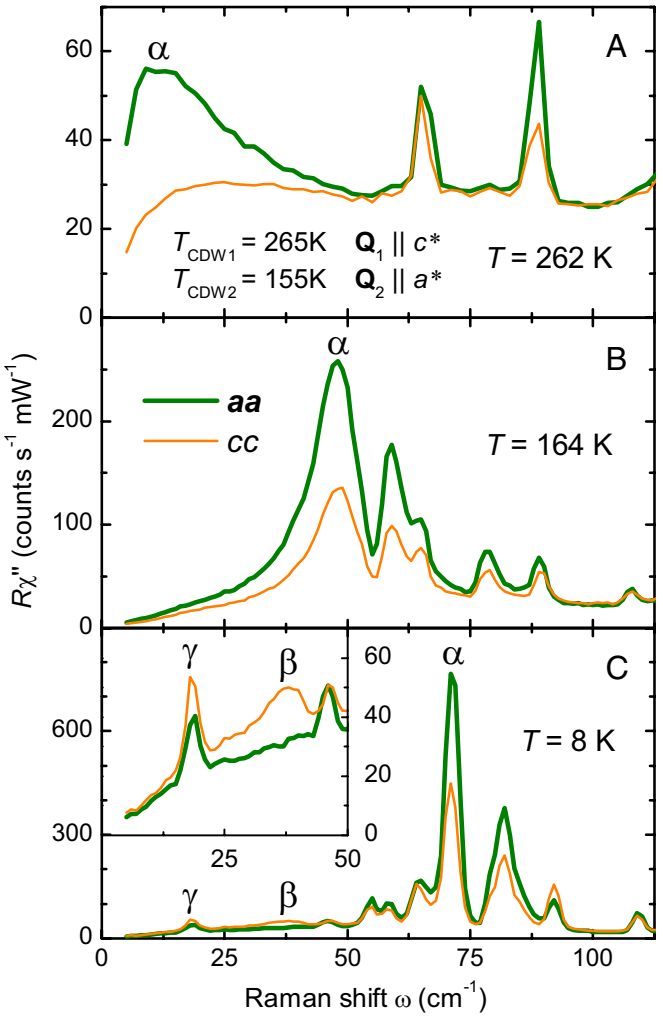

Fig. 3. Amplitude modes of $ErTe_3$ for the two CDW transitions. The three panels show comparisons of the *aa* and *cc* polarized spectra at selected temperatures. Note the different intensity scales. *c** and *a** are reciprocal lattice vectors parallel to the crystallographic lattice vectors *c* and *a*, respectively. The amplitude mode (peak-α) of the first transition displays a ~2:1 intensity ratio between the *aa* and *cc* polarizations, whereas the second AM (peak-β) is fully *cc*-polarized. *C Inset* shows the second amplitude mode (peak-β) and beat mode (peak-γ) at 18 cm^{-1} on an expanded intensity scale.

lowest temperature, it saturates at $\omega_{AM} = 71$ cm^{-1} (Fig. 3*C*, peak-α). The relation $\omega_{AM} = \sqrt{\lambda}\omega_{2\mathbf{k}_F}$ (2) at $T = 0$ between the energy of the AM and the unrenormalized CDW phonon energy ($\omega_{2k_F} = 110 \pm 20$ cm^{-1}) (16) leads to $\lambda = 0.4 \pm 0.1$. In contrast to superconductors, $\lambda = 0.4$ is already in the strong coupling regime, because it is well beyond the threshold of 0.103, which separates nematic from stripe order (5). As shown in Fig. 3*C Inset*, the second AM (peak-β) is fully *cc*-polarized and saturates at 38 cm^{-1}. Another mode (peak-γ in Fig. 3*C*) with resolution-limited width appears at $\Omega_\delta \sim 18$ cm^{-1}. The full analysis yields tetragonal B_{1g} symmetry, and the energy corresponds to the beat frequency of the two amplitude modes $\Omega_{beat} = 1/2|\Omega_{AM1} - \Omega_{AM2}|$ to within the experimental error. Microscopically, the coupling between collective states may result from eigenvector mixing, or it might be because the two condensates share common parts of the Fermi surface (28–30).

Temperature Dependence and Anisotropy of the CDW Gap. Fig. 4 depicts the electronic Raman response of $ErTe_3$ at various temperatures below T_{CDW1}. The spectra at 262 K (Fig. 4*A*) are isotropic, rise almost linearly between 800 and 3,500 cm^{-1}, and finally, become flat. On lowering the temperature, there is a transfer of spectral weight in the *aa* spectrum from low to high energies (Fig. 4 *B* and *C*). At 8 K (Fig. 4*C*), there is a relatively weak new structure in the *cc* spectrum in the range 500–1,200 cm^{-1}. Fig. 4*C Insets* highlights the temperature dependences of the *aa* and *cc* polarized spectra right above and below T_{CDW1} and T_{CDW2}, respectively. In either case, spectral weight is progressively suppressed below the gap edges and piles up above. As opposed to the AMs (Fig. 3), there is a full anisotropy without any leakage between the two orthogonal *aa* and *cc* directions, indicating that the crystal is single domain in the probed spot.

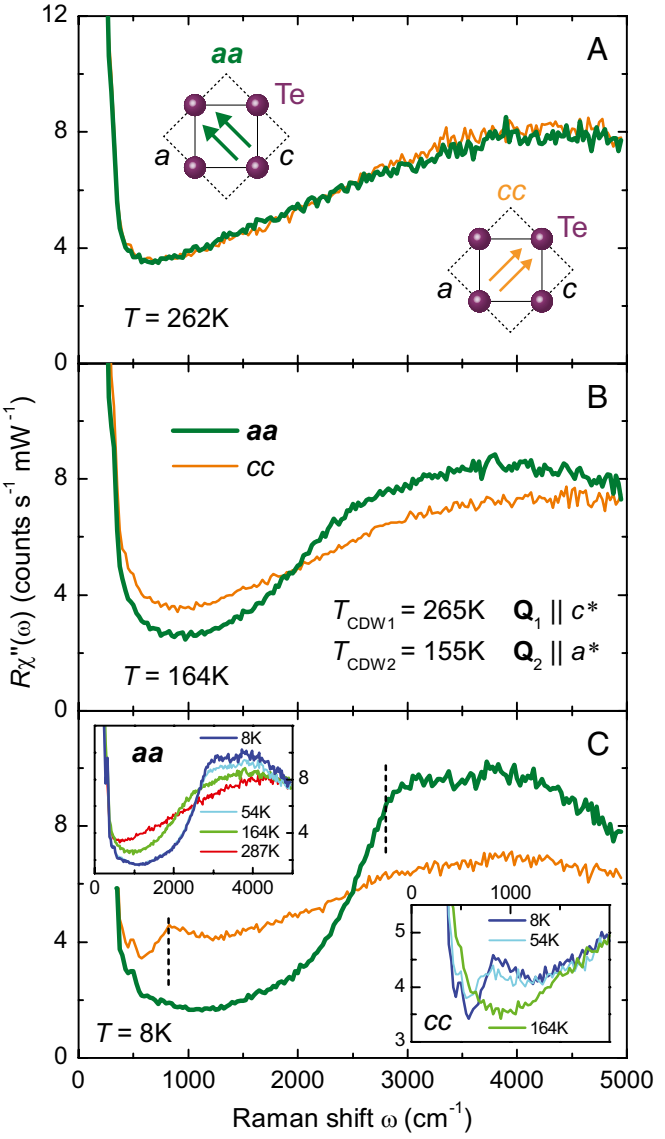

Fig. 4. Temperature dependence of the high-energy Raman spectra in $ErTe_3$. (*A*) At 262 K, there is no difference in the electronic excitations at high energy for both polarizations. *A Insets* sketch the incoming and scattered photon polarizations (defined in *Materials and Methods*). (*B*) At 164 K, the anisotropy between the two polarizations is already well-resolved. (*C*) In the limit $T \to 0$, the electronic gaps with edges at 800 and 2,800 cm^{-1} (dashed lines) for both CDWs are fully developed. *C Insets* show the temperature dependences of both CDW gaps using the same color code. Note that the signatures of the CDW transition at T_{CDW1} with $\mathbf{Q}_1 \parallel c^*$ are observed with incoming and scattered light polarizations parallel to *a*. The opposite is true for the transition at T_{CDW2}, which is shown in detail in Fig. 5.

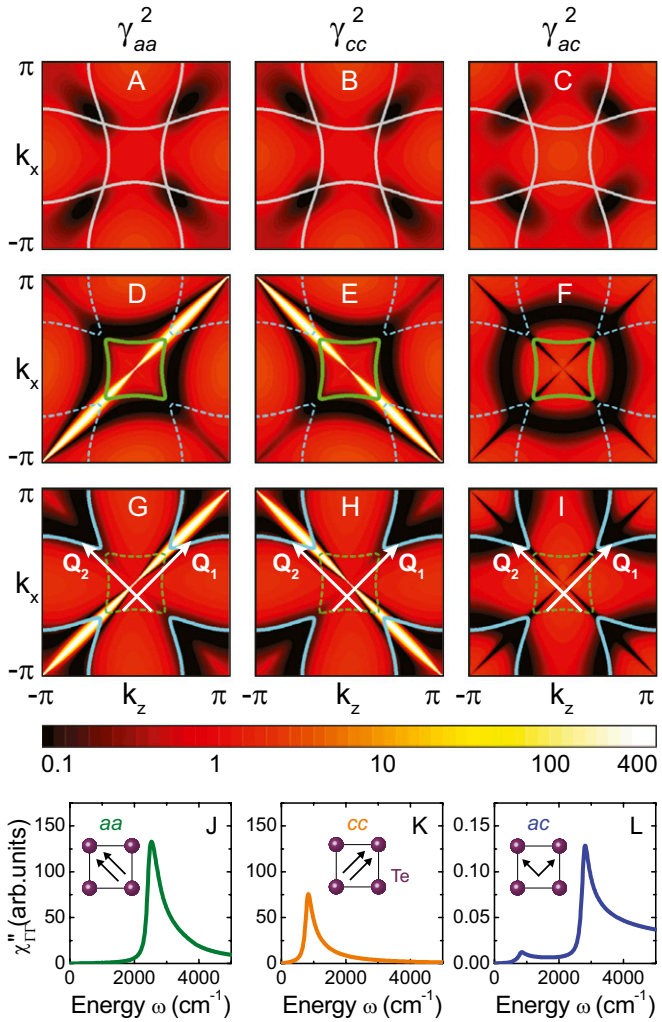

Fig. 5. Theoretical prediction for the Raman vertices and spectra of $ErTe_3$. (*A–I*) All vertices are derived from the band structure according to Eq. **S2**. *A–C* show the vertices without 2D coupling ($V_{xz} = 0$) and the corresponding Fermi surfaces. Raman vertices for the bands corresponding to (*D–F*) the central part of the Fermi surface (green) and (*G–I*) the outer part (light blue). The focusing effect caused by the lifted degeneracy enhances the vertices by more than two orders of magnitude, which is indicated by the color code. The ordering vectors are displayed in *G–I*. (*J–L*) All spectra are calculated at $T < T_{CDW2}$ and include both CDWs (Eq. **S2**). (*J* and *K*) For parallel polarizations, one observes only the CDW with ordering vector perpendicular to the light polarizations. The response of the respective orthogonal CDW is too weak to be visible. (*L*) For *ac* polarization, both gaps can be resolved, but the overall intensity is more than three orders of magnitude lower than the intensity in the two other configurations. This intensity is well below the detection limit, and in fact, no signatures of the gaps can be observed experimentally in *ac* polarization (Fig. S2).

Single-domain areas were already observed in an earlier angle-resolved photoemission spectroscopy (ARPES) experiment on $ErTe_3$ (31). We identify the edges with two times the maximum gap energies of the first and the second CDWs, $2\Delta_1 = 2{,}800$ cm^{-1} and $2\Delta_2 = 800$ cm^{-1}, respectively, in agreement with ARPES findings (31).

Raman Selection Rules and Anisotropic Electron–Lattice Coupling. We now elaborate on the remarkable selection rules described in the preceding paragraph (Fig. 4) and relate them to hybridization effects of the band structure. In addition and more importantly, we show that the selection rules and the strong anisotropy of the electron–phonon coupling, which influences the CDW ordering, are intimately connected and just two sides of the same coin.

The electronic Raman response, including the selection rules, can be derived directly from the band structure and the momentum dependences of the CDW gaps using the formalism in the work by Ványolos and Virosztek (32). The intensity of the light scattering for different polarization combinations (Raman vertices) are mainly determined by the curvature of the electronic dispersion, which is described in detail in ref. 33. If we neglect hybridization ($V_{xz} = 0$) (Fig. 1*B*), the Raman vertices are almost featureless, with little highlights in particular regions of the Fermi surface, which is illustrated in Fig. 5 *A–C* for the *aa*, *cc*, and *ac* polarizations, respectively. On including hybridization, the band degeneracy is lifted (Fig. 1*D*), and the two bands exhibit strong curvatures (Fig. 1*D* and Fig. S1). As a result, the vertices become highly focused along the diagonals of the Brillouin zone for parallel polarizations, which is shown in Fig. 5 *D*, *E*, *G*, and *H* for both bands because of nearly singular band curvature (34). This focusing enhances the light scattering precisely at the Fermi surface points connected by the CDW ordering wave vectors.

The focusing effect on the electronic spectra can be shown directly through the weak-coupling Raman response $\chi''_{\Gamma,\Gamma}$ (Eq. **S8**). We assume that, at $T < T_{CDW2}$, the two perpendicular CDWs with ordering vectors $\mathbf{Q_1}$ and $\mathbf{Q_2}$ have fully developed gaps Δ_1 and Δ_2, respectively. The $\mathbf{Q_1}$ and $\mathbf{Q_2}$ vectors connect the corners of the electron pocket around the Γ-point with the corners of the hole pockets (Figs. 1 and 5). The response for the *aa*, *cc*, and *ac* polarization orientations is shown in Fig. 5 *J–L*. No mixing can be observed in the spectra with parallel polarizations (Fig. 5 *J* and *K*). In the *ac* configuration, both gaps are, in principle, visible (Fig. 5*L*), but the expected intensity is three orders of magnitude smaller than in *aa* and *cc* and cannot be observed in the experiment (Fig. S2).

Because we do not include any other scattering mechanisms, phase space restricts the nonresonant creation of electron–hole excitations to points where the CDW mixes particles with wave vectors $\mathbf{k}$ and $\mathbf{k} + \mathbf{Q}$ across the Fermi surface. Consequently, light scattering is enhanced where energy is gained because of the CDW gap opening at the Fermi surface (Fig. 5 *J–L*). Raman scattering efficiently projects out the relevant parts of the Brillouin zone in such a multiband system; therefore, the signal is small at low energies below the gap edge, but it is significantly enhanced at two times the CDW gap (Fig. 5 *J–L*), which is in agreement with our experiment (Fig. 4*C*).

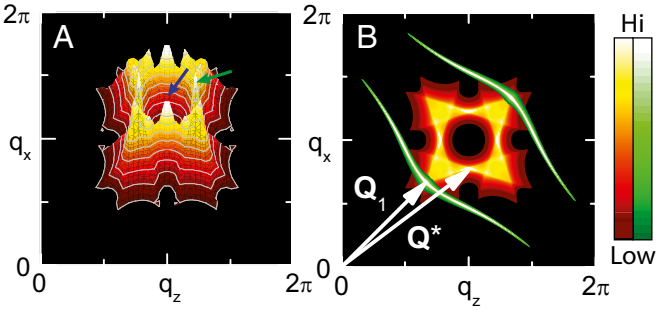

Fig. 6. Comparison of the susceptibilities. (*A*) 3D plot of the real part χ'_L of the Lindhard susceptibility. There is little structure around the rim. There are two orthogonal but equivalent ordering directions **Q*** as indicated by blue and green arrows. (*B*) 2D superposition of the real parts of the Lindhard susceptibility (χ'_L, yellow to red) and the projected susceptibility for interband scattering transitions (χ'_P, green). For clarity, only one ordering direction is shown. It is the focusing effect of the stress tensor that selects the experimentally observed ordering wave vector $\mathbf{Q_1}$.

Obviously, the lifting of band degeneracies dramatically affects the Raman selection rules by locally enhancing the Raman vertex (Fig. 5), which is proportional to the inverse effective mass tensor (33). Now, we make use of an analogy between electron–phonon and electron–photon scattering, where the electrons scatter from a phonon rather than a photon and the electron–phonon coupling vertex replaces the Raman vertex (35). In particular, for the case of stress phonons, the electron–phonon coupling vertex is given by the electronic stress tensor, which is proportional to the inverse effective mass tensor (36–39). As a result, for the system studied here, the electron–phonon coupling vertex, like the Raman vertex, is highly anisotropic in momentum space. Although the Lindhard susceptibility χ_L is relevant for a momentum-independent electron–phonon coupling, in this case, we must include the momentum-dependent electron–phonon coupling vertex into the electronic susceptibility; we call this susceptibility χ_P (*Materials and Methods* and *SI Text*) (40). Fig. 6 illustrates the importance of including the electron–phonon coupling vertex, where we compare the real parts χ_L' and χ_P' of both susceptibilities. Whereas the Lindhard susceptibility χ_L' has maxima of comparable height for several different ordering vectors (Fig. 6*A*) and therefore, does not lead to an unambiguous selection of one of them, χ_P' contributes to the instability at the proper location in $\mathbf{q}$ space and finally, selects the experimentally observed ordering vector $\mathbf{Q_1}$ (Fig. 6*B*). Here, $\mathbf{q}$ is the difference of the momenta $\mathbf{k}$ and $\mathbf{k}'$ of a scattered electron. Furthermore, as noted in the work by Yao et al. (5), any enhancement of the averaged electron–phonon coupling strength λ (definition in *SI Text*) will drive the system farther to the observed order. These two effects conspire to minimize the dependence on model details.

Discussion

The huge modulation of the Raman vertex indicates strong fluctuations of the charge density in the vicinity of the degeneracy points. These fluctuations manifest themselves in the Raman response above T_{CDW1} (Fig. 2), where the lattice still has the full C_4 symmetry. The work by Yao et al. (5) showed, in the framework of a Landau expansion of the free energy, that both charge fluctuations and electron–phonon coupling cooperate to drive the system to the experimental ordering vector. The substantial charge fluctuations couple to and soften the phonon relevant for the CDW ordering. Taking into account the large electron–phonon coupling near the band degeneracy points (Fig. 5), the charge fluctuations actually renormalize the phonon frequency at the momenta $\mathbf{q} = \mathbf{Q_1}(\mathbf{Q_2})$ rather than $\mathbf{Q^*}$ (and the equivalent orthogonal vector). Below T_{CDW1}, the weak orthorhombicity along with the relatively large electron–phonon coupling (5) then tips the balance, and $\mathbf{Q_1}$ aligns along c^* rather than a^*. Finally, on additional lowering, the temperature below T_{CDW2} $\mathbf{Q_2}$ aligns along a^*, because the Fermi surface along the c^* direction is already fully gapped by the first transition (13, 31).

Therefore, we identify two cooperating effects determining the overall selection of the ordering vector. (*i*) The system gains energy by gapping the band degeneracy points on the Fermi surface where the Raman selection rules indicate substantial fluctuations with fourfold symmetry above T_{CDW1}. (*ii*) Since the electron–phonon coupling vertex is proportional to the Raman vertex for stress phonons (36, 38), both quantities are enhanced near band degeneracies. For small hybridization and an electron–phonon coupling strength of $\lambda > 0.5$, the focusing effect may even be the most relevant contribution to the phonon renormalization (thus, the CDW formation), whereas it is only a correction for larger V_{xz}. Hence, although electron–phonon coupling is known to be important in CDW systems (3–5), we identify on a microscopic basis the focusing effect to be a more generic paradigm for multiband materials. As a future outlook, it seems particularly interesting to explore this novel scenario in the proximity of superconductivity, eventually competing or coexisting with CDW order. In fact, superconductivity appears at ∼2 K in some of the rare-earth tritellurides if the CDW is suppressed by applied pressure (41, 42). Moreover, it would be intriguing to address in a wider context the effects of band hybridization in materials such as the iron-based superconductors (34), in which density-wave order and superconductivity interplay on a microscopic scale.

Materials and Methods

Samples and Experimental Technique. Well-characterized single crystals of $ErTe_3$ were grown by slow cooling of a binary melt as described elsewhere (11, 13). $ErTe_3$ is a particularly well-ordered system. In the *a*–*c* plane, the resistivity varies only slowly above T_{CDW1} and is very small in the $T = 0$ limit (13). The crystals were cleaved before being mounted into the cryostat.

The imaginary part $R\chi''_{i,s}(\omega, T)$ of the Raman response is measured for various polarization combinations of incoming and scattered photons (e_i and e_s) referred to as *aa*, *cc*, and *ac* using Porto notation. Symbolic representations by two arrows in the Te plane are shown along with the spectra. Usually, more than one symmetry component is projected out at a given polarization e_i, e_s. The pure symmetries correspond to specific eigenvectors in the case of phonons and separate regions in the Brillouin zone for electron-hole excitations (33). In this publication, we show predominantly spectra with *aa* and *cc* polarizations, which comprise A_{1g} and B_{1g} symmetry components in a tetragonal lattice and the A_g symmetry on an orthorhombic lattice. In either case, the response has C_2 symmetry.

For the experiments, we made use of a solid-state laser emitting at 532.3 nm (KLASTECH SCHERZO) for excitation. The absorbed laser power ranged from 1 to 2 mW to keep the local heating below 5 K in the 50 × 100 μm^2-sized focus. The spectra were measured with a resolution of 2.5 cm^{-1} at low energy and 20 cm^{-1} at high energy. The Raman response $R\chi''$ is then obtained by dividing the measured spectra by the thermal Bose factor $\{1 + n(\omega, T)\} = [1 - e^{-\hbar\omega/k_BT}]^{-1}$. R is a constant that absorbs experimental factors and takes care of the units.

Theory. As noted here, the anisotropic electron–phonon coupling vertex must be included in the electronic susceptibility. For the case of stress phonons, the electron–phonon coupling and Raman vertices are related by $g_k = g\gamma_k$ (36, 39), where g sets the strength of the overall electron–phonon interaction. We, therefore, define the projected electronic susceptibility as

$$\chi_P(q, \Omega) = 2\sum_k \gamma_k^+\gamma_k^- \frac{f(\epsilon^+_{k+q/2}) - f(\epsilon^-_{k-q/2})}{\Omega + i\delta + \epsilon^+_{k+q/2} - \epsilon^-_{k-q/2}}, \quad [1]$$

where $\epsilon_k^\pm$ are the two bands and $\gamma_k^\pm = \gamma_{aa}^\pm + \gamma_{cc}^\pm$ are the fully symmetric effective mass vertices derived in *SI Text*. We consider only interband contributions that are generally accentuated by nesting as shown in Fig. 1*C*. Here, we wish to explore how nesting and anisotropic electron–phonon coupling conspire to ultimately select the experimentally observed ordering vector $\boldsymbol{Q_1}$. $\chi_P(q, \Omega)$ leads to a significant phonon softening at the wave vector $\boldsymbol{Q_1}$ connecting the corners of the Fermi surface, where the band degeneracy is lifted. The effect is very sensitive to the hybridization parameter V_{xz}. Results for a set of hybridization parameters are shown in Fig. S3.

ACKNOWLEDGMENTS. We benefited from discussions with B. Moritz, R. G. Moore, and B. Muschler and thank T. Böhm for assistance. R.H. thanks the Stanford Institute for Materials and Energy Sciences, where part of the paper was completed, for its hospitality. A.F.K. and T.P.D. thank the Walther Meißner Institut for its hospitality. Financial support from Deutsche Forschungsgemeinschaft Grant HA 2071/5-1 and the Collaborative Research Center TRR 80 is gratefully acknowledged. L.D. acknowledges support by the Swiss National Foundation for the Scientific Research within the pool, "Materials with Novel Electronic Properties" of the National Centres of Competence in Research network. E.A.N., A.F.K., T.P.D., J.-H.C., J.G.A., and I.R.F. acknowledge support from US Department of Energy, Basic Energy Sciences, Materials Sciences and Engineering Division Contract No. DE-AC02-76SF00515.

1. Kohn W (1959) Image of the Fermi surface in the vibration spectrum of a metal. *Phys Rev Lett* 2(9):393–394.
2. Grüner G (1994) *Density Waves in Solids*, ed Pines D (Addison–Wesley, Reading, MA).
3. McMillan WL (1977) Microscopic model of charge-density waves in 2*H*-$TaSe_2$. *Phys Rev B* 16(2):643–650.
4. Varma CM, Simons AL (1983) Strong-coupling theory of charge-density-wave transitions. *Phys Rev Lett* 51(2):138–141.
5. Yao H, Robertson JA, Kim EA, Kivelson SA (2006) Theory of stripes in quasi-two-dimensional rare-earth tellurides. *Phys Rev B* 74(24):245126.
6. Kiss T, et al. (2007) Charge-order-maximized momentum-dependent superconductivity. *Nat Phys* 3:720–725.
7. Johannes MD, Mazin II (2008) Fermi surface nesting and the origin of charge density waves in metals. *Phys Rev B* 77(16):165135.
8. Weber F, et al. (2011) Extended phonon collapse and the origin of the charge-density wave in 2*H*-$NbSe_2$. *Phys Rev Lett* 107(10):107403.
9. Lamago D, et al. (2010) Measurement of strong phonon softening in Cr with and without Fermi-surface nesting by inelastic x-ray scattering. *Phys Rev B* 82(19):195121.
10. Heid R, et al. (2000) Anomalous lattice dynamics of ruthenium. *Phys Rev B* 61(18): 12059–12062.
11. Ru N, Fisher IR (2006) Thermodynamic and transport properties of YTe_3, $LaTe_3$, and $CeTe_3$. *Phys Rev B* 73(3):033101.
12. Brouet V, et al. (2008) Angle-resolved photoemission study of the evolution of band structure and charge density wave properties in RTe_3 (R = Y, La, Ce, Sm, Gd, Tb, and Dy). *Phys Rev B* 77(23):235104.
13. Ru N, et al. (2008) Effect of chemical pressure on the charge density wave transition in rare-earth tritellurides RTe_3. *Phys Rev B* 77(3):035114.
14. Yusupov RV, Mertelj T, Chu JH, Fisher IR, Mihailovic D (2008) Single-particle and collective mode couplings associated with 1- and 2-directional electronic ordering in metallic RTe_3 (R=Ho,Dy,Tb). *Phys Rev Lett* 101(24):246402.
15. Schmitt F, et al. (2008) Transient electronic structure and melting of a charge density wave in $TbTe_3$. *Science* 321(5896):1649–1652.
16. Lavagnini M, et al. (2008) Evidence for coupling between charge density waves and phonons in two-dimensional rare-earth tritellurides. *Phys Rev B* 78(20):201101.
17. Lavagnini M, et al. (2010) Raman scattering evidence for a cascade evolution of the charge-density-wave collective amplitude mode. *Phys Rev B* 81(8):081101.
18. Pfuner F, et al. (2010) Temperature dependence of the excitation spectrum in the charge-density-wave $ErTe_3$ and $HoTe_3$ systems. *Phys Rev B* 81(19):195110.
19. Lazarević N, Popović ZV, Hu R, Petrovic C (2011) Evidence of coupling between phonons and charge-density waves in $ErTe_3$. *Phys Rev B* 83(2):024302.
20. Hu BF, et al. (2011) Optical study of the multiple charge-density-wave transitions in $ErTe_3$. *Phys Rev B* 84(15):155132.
21. Emery VJ, Kivelson SA, Lin HQ (1990) Phase separation in the *t-J* model. *Phys Rev Lett* 64(4):475–478.
22. Marder M, Papanicolaou N, Psaltakis GC (1990) Phase separation in a *t-J* model. *Phys Rev B* 41(10):6920–6932.
23. Grilli M, Raimondi R, Castellani C, Di Castro C, Kotliar G (1991) Superconductivity, phase separation, and charge-transfer instability in the U=∞ limit of the three-band model of the CuO_2 planes. *Phys Rev Lett* 67(2):259–262.
24. Kivelson SA, et al. (2003) How to detect fluctuating stripes in the high-temperature superconductors. *Rev Mod Phys* 75(4):1201–1241.
25. Kostur VN (1992) Electron Raman-scattering in metals with strong electron-phonon coupling. *Z Phys B* 89(2):149–159.
26. Caprara S, Di Castro C, Grilli M, Suppa D (2005) Charge-fluctuation contribution to the Raman response in superconducting cuprates. *Phys Rev Lett* 95(11):117004.
27. Benfatto L, Caprara S, Di Castro C (2000) Gap and pseudogap evolution within the charge-ordering scenario for superconducting cuprates. *Eur Phys J B* 17(1):95–102.
28. Littlewood PB, Varma CM (1981) Gauge-invariant theory of the dynamical interaction of charge density waves and superconductivity. *Phys Rev Lett* 47(11):811–814.
29. Browne DA, Levin K (1983) Collective modes in charge-density-wave superconductors. *Phys Rev B* 28(7):4029–4032.
30. Tüttö I, Zawadowski A (1992) Theory of Raman scattering of superconducting amplitude modes in charge-density-wave superconductors. *Phys Rev B* 45(9):4842–4854.
31. Moore RG, et al. (2010) Fermi surface evolution across multiple charge density wave transitions in $ErTe_3$. *Phys Rev B* 81(7):073102.
32. Ványolos A, Virosztek A (2005) Electronic Raman scattering in unconventional density waves. *Phys Rev B* 72(11):115119.
33. Devereaux TP, Hackl R (2007) Inelastic light scattering from correlated electrons. *Rev Mod Phys* 79(1):175–233.
34. Mazin II, et al. (2010) Pinpointing gap minima in $Ba(Fe_{0.94}Co_{0.06})_2As_2$ via band-structure calculations and electronic Raman scattering. *Phys Rev B* 82(18):180502.
35. Devereaux TP (1992) Theory for the effects of impurities on the Raman spectra of superconductors. *Phys Rev B* 45(22):12965–12975.
36. Shastry BS, Shraiman BI (1990) Theory of Raman scattering in Mott-Hubbard systems. *Phys Rev Lett* 65(8):1068–1071.
37. Einzel D, Klam L (2008) Response, relaxation and transport in unconventional superconductors. *J Low Temp Phys* 150(1-2):57–81.
38. Miller PB, Axe JD (1967) Internal strain and Raman-active vibrations in solids. *Phys Rev* 163(3):924–926.
39. Keck B, Schmid A (1976) Superconductivity and electron-phonon interaction in impure simple metals. *J Low Temp Phys* 24(5-6):611–629.
40. Varma CM, Weber W (1977) Phonon dispersion in transition metals. *Phys Rev Lett* 39 (17):1094–1098.
41. Hamlin JJ, et al. (2009) Pressure-induced superconducting phase in the charge-density-wave compound terbium tritelluride. *Phys Rev Lett* 102(17):177002.
42. Maple MB, et al. (2012) Superconductivity, spin and charge order, and quantum criticality in correlated electron materials. *EPJ Web of Conferences* 23:00012.